Journal of the European Ceramic Society 46 (2026) 118222

Contents lists available at ScienceDirect

Journal of the European Ceramic Society

journal homepage: www.elsevier.com/locate/jeurceramsoc

Chemical composition and structural evolution of surface passivation film in rare earth high-entropy Ti-pyrochlore

Minghao Zhao [a], Kun Yang [a,b,*], Wangwei Ru [a], Hao Ji [a], Yibo Wang [a], Wei Chen [a], Xiaobin Tang [a,b]

[a] Department of Nuclear Science and Technology, Nanjing University of Aeronautics and Astronautics (NUAA), Nanjing 211106, China
[b] Key Laboratory of Advanced Nuclear Technology and Radiation Protection, Ministry of Industry and Information Technology, Nanjing 211106, China

ARTICLE INFO

Keywords:
Pyrochlore
Passivation film
Dissolution-reprecipitation
Chemical durability

ABSTRACT

The passivation behavior of polycrystalline structural ceramics under extreme corrosion conditions is critical for future advanced energy applications, including nuclear waste immobilization. The current study investigated the chemical durability of the high-entropy pyrochlore rare earth Ti pyrochlore (HE-$RE_2Ti_2O_7$) by focusing on the fundamental understanding of the nexus between chemical composition and the structural evolution of the surface formation of passivation film. Results provide evidence to support that the formation of a multilayer surface passivation film enriched in both A and Ti elements is associated with a dissolution-reprecipitation mechanism, which is strongly associated to the metal-oxygen bonding strength. The formation of passivation film dominated by the synergistic effect of localized bonding environment led to dynamic transition between congruent and incongruent leaching mechanisms, and further affect the chemical durability. These findings establish a framework for designing corrosion-resistant nuclear waste forms by focusing on its surface alteration behavior through tuning the chemical composition.

1. Introduction

Pyrochlore ceramics ($A_2B_2O_7$) have garnered significant interest in advanced energy applications, such as nuclear waste immobilization, catalysis, and high-temperature protection, owing to their structurally tunable pyrochlore framework (space group Fd $\bar{3}m$), outstanding radiation resistance, and robust chemical stability [1–3]. However, single-component pyrochlores underwent a sequential phase transformation process of "pyrochlore→fluorite→amorphous" ultimately leading to structural collapse subjected to an extremely corrosive environment [4].

Despite the effect of localized metal-oxygen bond strength on the chemical durability of the crystalline structure materials [5], the dynamic evolution of the surface alteration layer during corrosion plays a decisive role in long-term material stability [6–8]. The chemical composition, microstructural property, and dynamic evolution of passivation layers directly affect elemental transport kinetics at solid/-liquid interfaces, as denoted in previous research [9,10]. The formation mechanisms of alteration layers in oxide ceramics are analogous to those observed in glass systems, primarily governed by two distinct mechanisms according to literature studies [11]: Dissolution Reorganization Mechanism (DRM) involves in-situ structural reorganization of dissolved components through elemental dynamic migration at interfaces or defects, which was confirmed by the formation of silicon-rich porous hydrogel in borosilicate glasses subjected to neutral/weakly alkaline conditions through hydrolysis/polycondensation of Si-O bonds [12]. Similar phenomena are observed in conventional ceramic corrosion systems, such as silicon nitride (Si_3N_4), where dissolution of grain-boundary phases and subsequent reprecipitation of hydrated silica ($SiO_2{\cdot}nH_2O$) layers occur during acid or hydrothermal exposure [13]. For comparison, the coupled interface Dissolution-Reprecipitation (CIDR) mechanism suggests that dissolved components undergo recrystallization as a result of localized supersaturation near interfaces, accelerating the formation of secondary phases with distinct crystal structures accompanied by significant morphological evolution. This mechanism has successfully explained passivation layer formation in calcium titanate ceramics [14], with the amorphous passivation layer observed in $Er_2Ti_2O_7$ under acidic conditions also attributed to CIDR [4]. Although both mechanisms have been extensively supported by experimental evidence and theoretical simulations, the argument of

* Corresponding author at: Department of Nuclear Science and Technology, Nanjing University of Aeronautics and Astronautics (NUAA), Nanjing 211106, China.
E-mail address: kun.yang@nuaa.edu.cn (K. Yang).

https://doi.org/10.1016/j.jeurceramsoc.2026.118222
Received 1 August 2025; Received in revised form 3 December 2025; Accepted 6 February 2026
Available online 11 February 2026

whether dissolution-reorganization or dissolution- reprecipitation dominated has never stopped [4,15–17], particularly in multi-component pyrochlore (HE-$RE_2Ti_2O_7$) systems where the coupling effect of lattice distortion and surface alteration behavior strongly altered the bonding breakage and localize elemental diffusion. Previous studies by Yang et al. and Gin et al. have systematically investigated the coupled dissolution-intermediate reprecipitation (CDIR) mechanism in lanthanide titanates and oxide/glass composite systems, respectively [4, 16]. Till now, there is a lack of straightforward evidence that can link elemental leaching behavior to passivation layer evolution, leading to fundamental controversies in corrosion mechanism. Moreover, the potential nexus between lattice distortion and localized bonding environment still remains unknown.

Recent advancements in high-entropy ceramics (HECs) have revealed significantly enhanced corrosion and radiation resistance through multi-principal component synergy and lattice distortion effects, establishing a new paradigm for advanced ceramic design [18–20]. However, current research predominantly emphasizes the role of configurational entropy in thermodynamic stability [21–23], while few researchers have focused on the potential nexus between chemical disorder and surface passivation film. Although Zhou et al. [24] demonstrated suppression of large-radius cation release via lattice distortion, the potential surface alteration effect can have a significant impact on the chemical durability. Similarly, Teng et al. [25] explored dissolution behavior in single- to multi-component pyrochlores, yet the interfacial reaction mechanisms in multi-component systems remain unresolved. This knowledge gap critically impedes the development of corrosion-resistant high-entropy ceramics, especially for applications like nuclear waste immobilization in deep geological repositories.

Therefore, this study investigates the surface passivation formation and structural evolution of multi-component pyrochlore with uniform mixing entropy but diverse chemical disorder and crystalline structures. The surface alteration behavior and the passivation film formation mechanism were studied by oxygen isotope tracing ($^{18}O/^{16}O$) with depth profiling techniques through time-of-flight secondary ion mass spectrometry (TOF-SIMS). The microstructure evolution of the surface passivation film was further characterized by high-resolution transmission electron microscopy (HRTEM). The microstructure evolution, accompanied by the A-site and Ti elemental leaching behavior, can be used to explain the discrepancy in chemical durability. Overall, the current study helps clarify long-standing controversies regarding corrosion mechanisms and provides potential insights for designing nuclear waste immobilization materials in extreme environments, suggesting significant engineering value.

2. Materials and methods

2.1. Synthesis of HE-$RE_2Ti_2O_7$ ceramics

High-purity rare earth oxides (RE_2O_3, RE = La, Nd, Sm, Eu, Gsd, Dy, Ho, Er, Tm, Yb, Lu, Y) and titanium dioxide (TiO_2, ≥99.9 % purity, Macklin) were used as precursor materials to fabricate the pyrochlore. The stoichiometrically weighed powders were dried at 100 ℃ for 2 h to remove moisture. Wet ball milling was conducted in anhydrous ethanol using a planetary mill (MITR-YXQM, Changsha MITR Co., Ltd) with 5 mm zirconia balls at 500 rpm for 24 h. The slurry was filtered through 325-mesh sieve and vacuum-dried at 60 ℃ for 12 h.

The dried powder was pre-sintered in alumina crucibles using a muffle furnace (SG-XS1700, Shanghai Sager Co., Ltd.) with a heating rate of 5 ℃/min to 1100 ℃ (24 h dwell). The calcined powder was re-milled under identical conditions for 12 h, dried at 120 ℃ and sieved through 325-mesh.

Sample densification was achieved in a graphite die using a vacuum hot-press furnace (FHP-828, Suzhou Haatn Tech, China) at 1200 ℃, 50 MPa and 30 min under 10^{-3} Pa vacuum. Heating and cooling rates were controlled at 100 ℃/min. The sintered pellets were ground with SiC paper and mirror-polished with 0.25 μm diamond suspension. Bulk density was measured via Archimedes' principle using deionized water as an immersion medium. Theoretical density was calculated using Rietveld's refinement of XRD patterns. The SEM images (Fig. 2 and Figure S1) clearly denote that the as-fabricated ceramic sample pellets enjoy the similar grain size (~ 700 nm). The uniform grain size can eliminate the disruption of grain boundary dissolution or grain size effect on the ceramic chemical durability for the current study since the current study is solely focusing on the impact of chemical composition on the surface passivation film and chemical durability.

2.2. Structural characterization and composition analysis

The crystalline structure of the sample was performed using an X-ray diffractometer (XRD, Empyrean, Malvern Panalytical) with Cu Kα radiation (λ = 0.15406 nm). The diffraction patterns were recorded in the 2θ range of 10°–80° at ambient temperature, with the corresponding crystalline structure identified by MDI Jade (6.5). The chemical bond evolution of HE-$RE_2Ti_2O_7$ ceramics before and after leaching treatment was investigated by Raman spectroscopy (HORIBA HR Evolution, France). Measurements were conducted under 532 nm laser excitation with 10 s integration time, covering the spectral range of 200–1000 cm^{-1}.

High-resolution TEM imaging, selected area electron diffraction (SAED) patterns and elemental mappings were acquired to investigate the localized nanoscale structure evolution and elemental distribution via a Spectra 300 scanning transmission electron microscope (STEM, USA).

Surface composition depth profiling was conducted using time-of-flight secondary ion mass spectrometry (TOF-SIMS, TESCAN LYRA3 GMU, Tescan) to trace the dynamic migration behavior of oxygen isotopes ($^{18}O/^{16}O$). After a 25-day semi-dynamic leaching test in ^{18}O -enriched nitric acid solution (pH=1; prepared with 98 % ^{18}O-enriched water from Wuhan Isotope Technology Co., Ltd, Aladdin nitric acid, and deionized water), the oxygen isotope distribution within the surface passivation film was characterized via TOF-SIMS depth profiling, enabling spatial resolution of isotopic gradients across the altered layer. A 40 × 40 μm^2 area was sputter-etched with a focused Ga^+ ion beam (30 keV base setting, 4.5 nA beam current). Both positive and negative ion spectra were acquired, and elemental distribution maps were reconstructed using TOF-SIMS Explorer (1.4) software. Detailed experimental procedures are provided in the Supporting Information.

This study conducted comprehensive analyses of characteristic parameters in multi-component high-entropy ceramics, including average ionic radius, size disorder parameter (δ_{size}), mass disorder parameter (δ_{mass}), and mixing entropy to systematically investigate the structure property relationship in HE-$RE_2Ti_2O_7$ pyrochlore systems.

Five multi-component Ti-pyrochlore with identical mixing entropy and low to high average ionic radius were chosen from 16 candidate elements encompassing lanthanides (La–Lu) and Y to represent the effect of chemical disorder to structural evolution and further chemical durability (Table 1). Fig. 1 demonstrates the correlation between the average A-site ionic radius ($\overline{R}_A$). size disorder parameter (δ_{size}) and crystalline phases.

Table 1
Composition and property metrics of five high-entropy pyrochlore oxides.

Sample ID	Components	δ_{size} (%)	$\overline{R}_A$	$\overline{R}_A$ / R_{Ti}	δ_{mass} (%)
#HEC-1	$(DyErTmYbLu)_2Ti_2O_7$	1.74	0.997	1.649	2.60
#HEC-2	$(SmGdDyYbY)_2Ti_2O_7$	3.08	1.033	1.707	20.28
#HEC-3	$(NdSmEuHoLu)_2Ti_2O_7$	4.5	1.049	1.734	7.07
#HEC-4	$(LaNdErYbLu)_2Ti_2O_7$	7.05	1.047	1.731	9.46
#HEC-5	$(LaNdSmYbY)_2Ti_2O_7$	5.84	1.070	1.769	19.89

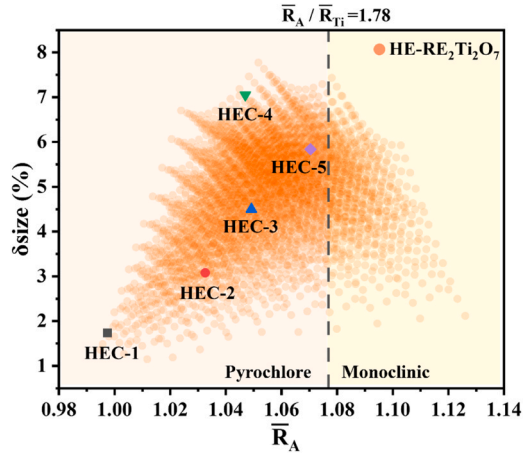

Fig. 1. Correlation between the average A-site ionic radius ($\overline{R}_A$) and size disorder (δ_{size}) in multi-component materials.

2.3. Chemical stability evaluation

The chemical durability of the high-entropy pyrochlore was assessed through a modified semi-dynamic leaching test based on ASTM C1308 [26]. The leachate enriched in ^{18}O was chosen to trace the surface alteration behavior and passivation film formation mechanism. The sample coupons were immersed in ^{18}O-enriched nitric acid solution (pH = 1) within PTFE sealed veal at 90 ℃ for 25 days, with a constant surface area-to-volume ratio (S/V) of 5.0 m^{-1} through leachate replenishment at day intervals.

The leachates were diluted by nitric acid before analysis. The concentrations of both A-site and Ti were analyzed via Inductive coupled plasma-mass spectroscopy ICP-MS (ICAP6300, USA). The elemental release rate m(i) [$mg{\cdot}m^{-2}{\cdot}d^{-1}$] was calculated as:

$$m(i) = \frac{C(i)V}{St} * Dilution\ factor \quad (1)$$

where $C(i)$ is the concentration of different ions ($mg{\cdot}L^{-1}$) measured by ICP-MS, the dilution factor is 100, t is the sampling interval (d), V is the volume of the leachate (L), and S is the surface area of the sample (m^2). The surface area to volume ratio (S/V) is a constant 5 m^{-1}.

The normalized leaching rate (L_N) was then derived as:

$$L_N = \frac{L}{Weight\ percent} \quad (2)$$

The cumulative quantity of the leached elements as a function of time was fitted using the Cote model [27], with the minimum R^2 achieved. The leaching kinetics of each element in the aqueous solution are described by the following empirical mathematical model according to the previous research [28]:

$$M(t) = k_1 t + k_2 t^{1/2} + k_3(1 - e^{-k_4 t}) \quad (3)$$

where M(t) represents the cumulative leaching rate, expressed in $mg{\cdot}m^{-2}$; $k_1 t$ denotes the mass dissolution controlled by the dissolution behavior; $k_2 t^{1/2}$ reflects the mass transport governed by the elemental diffusion; and $k_3(1 - e^{-k_4 t})$ accounts for the mass exchange between surface defects and the solute in the solution. The long-term leaching rate can then be derived by taking the derivative of the Cote model with respect to time and assuming that the leaching time approaches infinity, as denoted by k_1 [27].

3. Results

3.1. Microstructure, phase composition of the as-sintered HE-$RE_2Ti_2O_7$ ceramics

The cross-section microstructure of the as-fabricated sample coupons was characterized by SEM, with corresponding elemental mappings can be seen in Fig. 2. The average grain sizes of 657 nm were measured for the sample pellets, with homogeneous elemental distribution in single-phase pyrochlore (#HEC-3). For comparison, dual-phase pyrochlore (#HEC-4) denotes elemental segregation due to increased size disorder, which induces lattice distortion and monoclinic phase formation.

The XRD patterns of the as-fabricated multi-component ceramics are shown in Fig. 3. All five samples (#HEC-1 to #HEC-5) exhibited characteristic (331) and (531) peaks of the cubic pyrochlore structure at 2θ ≈ 38° and 52°, corresponding to the space group Fd $\overline{3}_m$. Notably, the #HEC-1, #HEC-2, and #HEC-3 samples showed no impurity peaks, indicating the formation of high-purity single-phase cubic pyrochlore structures (labeled as P-phase in Fig. 3a). In contrast, the #HEC-4 and #HEC-5 samples displayed additional diffraction peaks at 2θ ≈ 21° and 33°, attributed to the monoclinic phase [29] (M-phase, space group $P2_1/c$), confirming the coexistence of pyrochlore (P) and monoclinic (M) phase with increasing ionic radii.

The average A-site ionic radius ($\overline{R}_A$) increased from 0.997 Å (#HEC-1) to 1.070 Å (#HEC-5), causing a systematic shift of the strongest diffraction peak (2θ ≈ 32°) toward lower angles with the introduction of larger ionic radius elements (indicated by arrows in Fig. 3a), which can be explained by the Vegard's law [30], reflecting lattice expansion and an increase in interplanar spacing (d-value) due to solid solution formation. Rietveld refinement of the XRD data confirmed the successful synthesis of the high-entropy pyrochlore ceramic, as indicated by the agreement between the observed and calculated XRD profiles presented in Fig. 2c-e, along with the refined structural parameters provided in Table S1 and Fig. S2 (Supplementary Material).

Semi-quantitative analysis through Rietveld peak refinement of the XRD profiles subsequently revealed that the #HEC-4 and #HEC-5 samples contained 17.7 % and 57.3 % monoclinic phase, respectively (Fig. 3b). The average unit cell volume expanded from 1019 $Å^3$ to 1060 $Å^3$ as $\overline{R}_A$ increased as well. A phase transition from cubic to monoclinic occurs when the average R_A/R_B ratio exceeds 1.78, as the resulting lattice strain surpasses the stability limit of the cubic phase [4]. Localized enrichment of large A-site ions (e.g., La, Nd) may exacerbate this strain mismatch. While configurational entropy favors single-phase stabilization, the synergistic effects of size disorder δsize and electronegativity differences are equally crucial regarding to the phase competition. A distinguishable phase deviation can be seen for the $\overline{R}_A/R_{Ti}$ ratio of 1.73, which highlights the critical role of size disorder in driving phase separation (Fig. 3b). This structural complexity underscores the correlation between ionic radius mismatch and lattice stability in multi-component ceramics [23].

As revealed by Fig. 2, the monoclinic phase is dominated with larger lanthanide ions (La and Nd) at the A-site. In sample #HEC-4, the monoclinic phase constitutes 17.7 % of the material and primarily consists of a La/Nd-doped derivative of $Ln_2Ti_2O_7$ (Ln = La, Nd), with its A-site incorporating minor amounts of other rare-earth elements (REEs). Structurally, the monoclinic phase crystallizes in the $P2_1/c$ space group, which is characterized by distorted and tilted BO_6 octahedra.

Fig. 4a presents the Raman spectral of five high-entropy pyrochlore samples (#HEC-1, #HEC-2, #HEC-3, #HEC-4, #HEC-5), exhibiting vibrational modes of typical cubic pyrochlore phase. Specifically, the Eg peak at 300 cm^{-1} corresponds to Ti-O-Ti bending vibrations, the A_{1g} peak at 520 cm^{-1} arises from symmetric vibrations of TiO_6 octahedra, while F_{2g} peaks are observed at 230 cm^{-1} and 700 cm^{-1} (Fig. 4a), consistent with literature reports on cubic pyrochlore structures [31].

Notably, #HEC-4 and #HEC-5 samples display additional RE-O bond

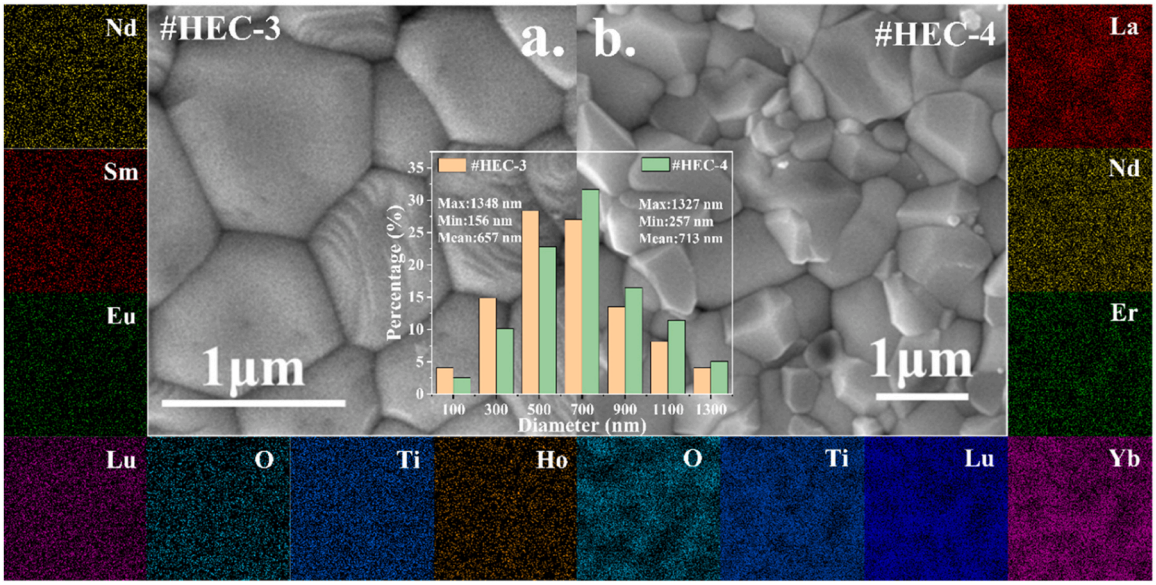

Fig. 2. Microstructure and elemental Mapping of pyrochlore in (a) Sample #HEC-3 and (b) Sample #HEC-4.

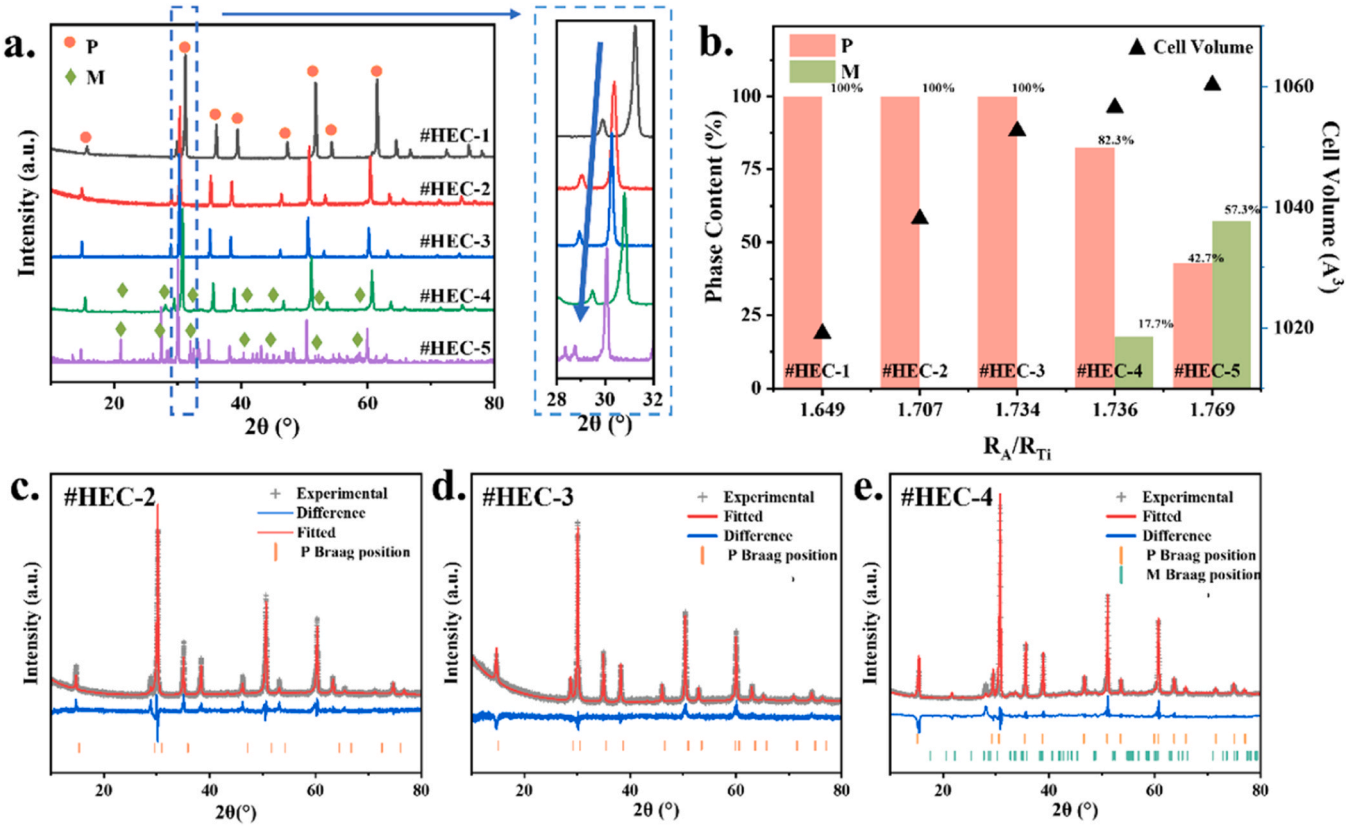

Fig. 3. Crystalline structure evolution of HE-$RE_2Ti_2O_7$ ceramics (a) Sample XRD profiles, (b) Phase content and cell volume versus $\overline{R}_A/R_{Ti}$, (c-e) Experimental versus fitted patterns for selected samples.

vibration peaks (labeled as RE-O(D) and RE-O(A)) associated with monoclinic phase formation, indicating distinct bonding interactions between A-site rare-earth elements and oxygen atoms. In addition, the presence of a monoclinic phase can be further evidenced by the emergence of B_{2g} TiO_2 modes at 750 cm^{-1} further corroborates [29]. High consistency can be seen for the Raman spectra with major Raman peaks retained (E_g, F_{2g}, A_{1g}) before and post-leaching test, indicating the high stability of the pyrochlore lattice structure (Fig. 4b-d).

Besides, substantial Raman peak intensity enhancement can be seen for the E_g and A_{1g}, which can be attributed to the Ti-O bond, suggesting the gradual formation of the Ti-enriched surface layer for the #HEC-2 (Fig. 4b). On the other hand, #HEC-4 sample featured with dual crystalline phases shows significant attenuation of RE-O bond vibration intensities after leaching (Fig. 4d). This attenuation may arise from surface dissolution-induced etching and amorphization processes, which disrupt the coordination environment of RE-O bonds.

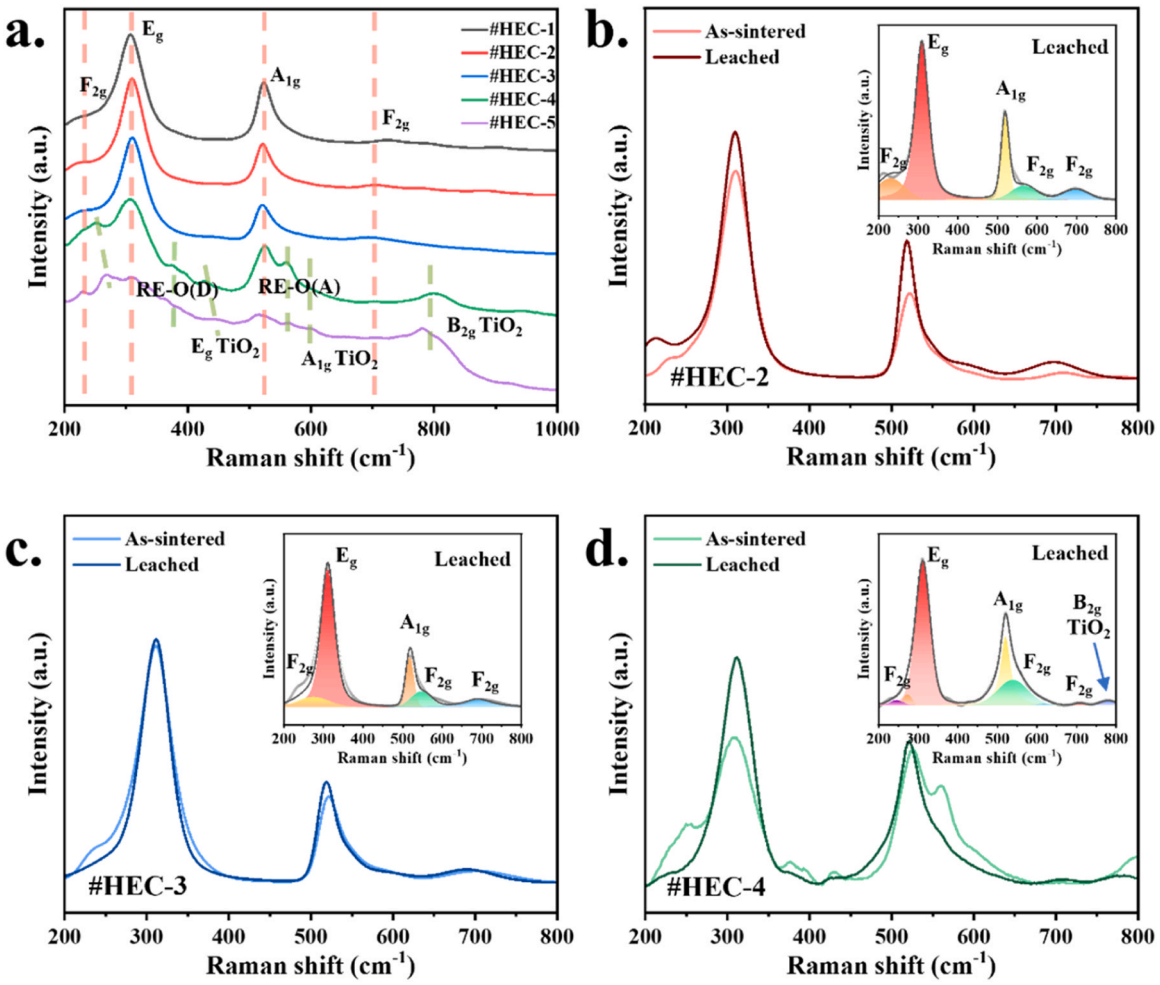

Fig. 4. Raman Spectra of As-Sintered and Leached Samples (a) Raman spectra of as-sintered samples. (b-d) Raman spectra of #HEC-2, #HEC-3, and #HEC-4 samples before and after leaching.

3.2. Microstructural evolution and surface passivation film formation of HE-$RE_2Ti_2O_7$ ceramics under semi-dynamic leaching

The nanoscale properties of the surface passivation film for #HEC-3 were further revealed by STEM (Fig. 5a). A platinum (Pt) protective layer covered on the top of the sample surface, followed by an amorphous passivation layer (~36.7 nm thick), with a crystalline altered matrix at the substrate, consistent with previous research [9]. The surface multilayer structure was further characterized by FFT patterns (Fig. 5b), which can be classified as follows: Region a.1 exhibits amorphous properties confirmed by halo rings. Region a.2 displays discrete diffraction spots corresponding to fluorite-structured phases. Region a.3 demonstrates both lattice fringes and diffraction spots unambiguously assigned to the pyrochlore structure. Therefore, the corrosion behavior of single-phase high-entropy pyrochlore underwent a stepwise corrosion pathway as follows: initial conversion from pyrochlore to fluorite structure precedes structural collapse and subsequent formation of passivation films.

The #HEC-3 sample exhibits a gradient decline of $^{18}O/^{16}O$ ratios with increasing depth until reaching the natural ^{18}O abundance level (0.205 %) at a penetration depth of 36.7 nm, consistent with the thickness of the passivation layer. These results further suggest the direct participation of ^{18}O isotopes in passivation film formation. Isotopic tracer analysis ($^{18}O/^{16}O$) combined with TEM observations strongly supports the dominance of the dissolution-reprecipitation mechanism in amorphous passivation layer formation. As illustrated in Fig. 5d, progressive ^{16}O enrichment at the film/matrix interface contrasts with ^{18}O predominance observed in the top surface region, demonstrating dynamic oxygen exchange with ^{18}O influx from the solution phase rather than static surface reconstruction.

The cross-section elemental mappings of the #HEC-3 were further denoted in Fig. 6. The A-site elemental depletion and oxygen-enriched in the top, especially the Ti, Eu, and Nd, can be attributed to the A-site rare earth elemental corrosion and diffusion, consistent with the leaching rates shown in Fig. 8. The thickness of the surface passivation film with A-site elemental depletion and oxygen-enriched around 36.7 nm is consistent with the $^{18}O/^{16}O$ profile in Fig. 5. Besides, the less depletion of Sm, Ho and Lu, as compared to Nd and Eu, consistent with the trend of ionic radii, further suggests the strong correlation with metal-oxygen (A-O) bonding strength.

The nanoscale microstructure analysis of #HEC-4 post-14-days' corrosion in a nitric acid solution containing ^{18}O-enriched water with large chemical disorder and dual crystalline phases was further evaluated by STEM (Fig. 7a). The grain boundary is visible, and a manifest large vacancy was observed, which can be attributed to the rapid grain dissolution corresponding to the monoclinic phase due to the corrosion. A rapid decline of $^{18}O/^{16}O$ atomic ratio within the top 40 nm followed by oscillatory fluctuations with increasing corrosion depth according to the TOF-SIMS in-depth profile (Fig. 7c). This fluctuation behavior can be mainly attributed to large vacancy formation and grain dissolution through monoclinic-phase dissolution, which accelerates ^{18}O penetration through the grain boundary, although the influence of oscillatory SIMS signals cannot be ruled out. The infiltrated ^{18}O subsequently underwent interfacial reactions with the subsurface pyrochlore phase,

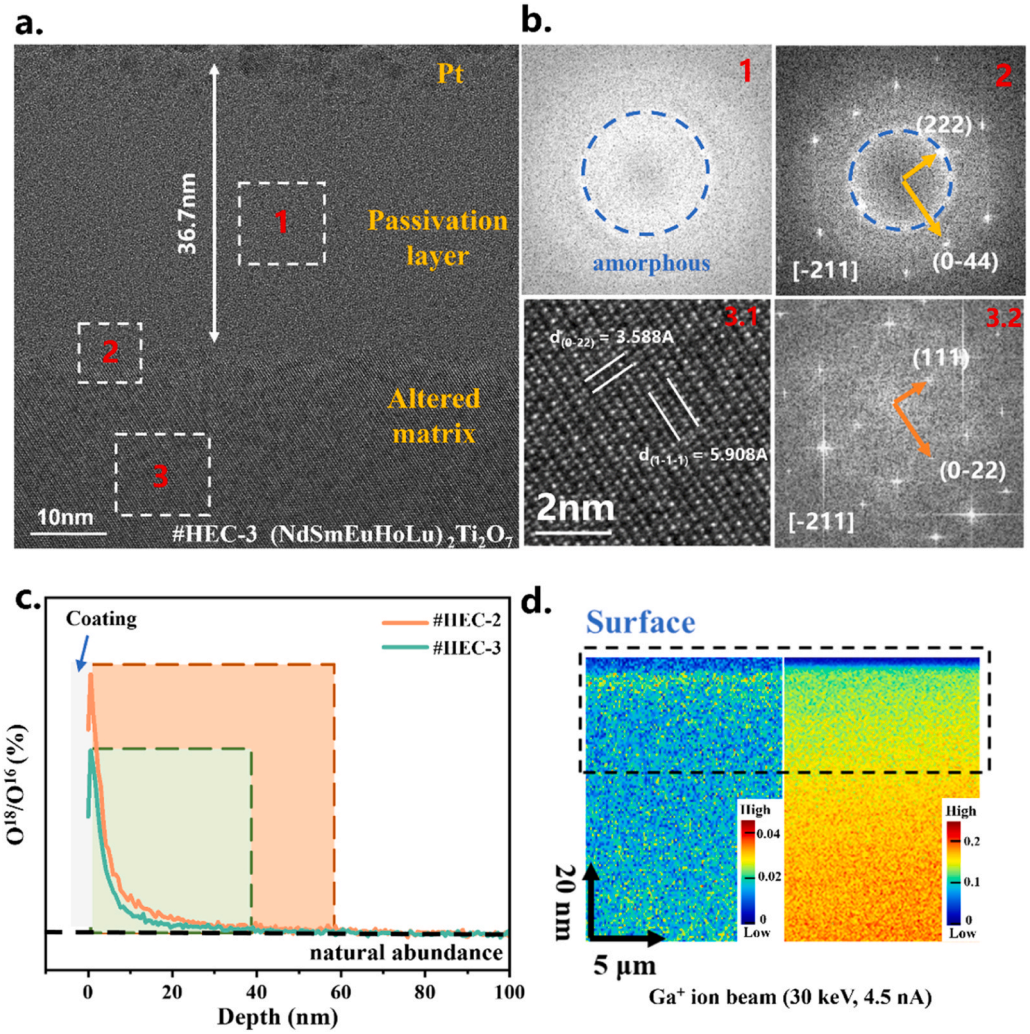

Fig. 5. Structural and Isotopic Analysis of the Passivation Layer (a) HRTEM image of the #HEC-3 passivation layer interface. (b) FFT and HRTEM images of the marked regions. (c) Oxygen isotope depth profile. (d) Oxygen isotope distribution map.

resulting in the formation of an amorphous layer on the edge of the grain according to the FFT pattern 6.

The corresponding crystalline structure evolution was further revealed by FFT patterns (Region 1–6). A crystalline structure with pyrochlore phase can be seen on region 1, with coexistence of fluorite and amorphous structure can be seen for the alteration layer region 2. The crystalline structure then disappeared and completely amorphized for the top alteration region 3, as denoted in Fig. 7. The stepwise structural evolution aligns well with the pyrochlore→-fluorite→amorphous phase transformation sequence, consistent with previously observed in the #HEC-3 sample. The significant grain sub-division occurred due to the interfacial corrosion along the grain boundary, as evidenced by the high-resolution STEM image in Region 2. Compared to the region e4, which maintains pyrochlore structure, the edge of the grain (region e5) can be indexed as fluorite phase, while nano grain with a diameter around 100 nm can be identified as a monoclinic structure coexists with the amorphous feature, further demonstrating the accelerate corrosion occurred in the monoclinic phase. The rapid dissolution of the monoclinic phase, as well as the rapid grain dissolution, can be further confirmed by the leaching rates in Fig. 9.

The depth profile of the surface alteration layer can be further analyzed by the positive ion mode TOF-SIMS (Fig. 8). The normalized A/Ti ratio remains < 1 within the surface 40 nm region (as indicated by the baseline A/Ti=1 in the inset) for #HEC-2 according to the depth profile, supporting the formation of a thin Ti-dominated amorphous passivation film. Localized A-site and Ti-enriched nano spots marked by red arrows can be seen from the top-view of the surface elemental mapping (Fig. 8b), while a top layer dominated by Ti, with few A-site element can be seen for #HEC-2 according to the cross-section elemental mapping, providing additional evidence for the dissolution-reprecipitation mechanism.

Compared to sample #HEC-2 with the low chemical disorder, higher passivation film thickness, featuring a bilayer structure, can be seen for #HEC-3. The surface passivation film with lean in A-site element and Ti-enriched, featured with bilayer property, can be seen for #HEC-3 according to the TOF-SIMS depth profile (Fig. 8c-d). The simultaneous bonding breakage of A-O and Ti-O leads to the rapid dissolution of both A-site element and Ti in nitric acid solution (pH=1), which facilitates the Ti reprecipitation back on the altered surface due to the low solubility as denoted in the depth profile. The larger ionic radius of A-site elements compared to sample #HEC-2 leads to faster A-O bonding breakage, which further accelerates the leaching of A-site elements. Although the Ti passivation layer provides a certain level of protective ability for the matrix underneath (Fig. 9a), the saturation of A-site element solubility at the interface induces localized precipitation, ultimately resulting in the observed bilayer passivation film with an A-enriched layer staying on the outward of the Ti-enriched film. The bilayer structure of the surface passivation film further supports the dissolution-reprecipitation mechanism.

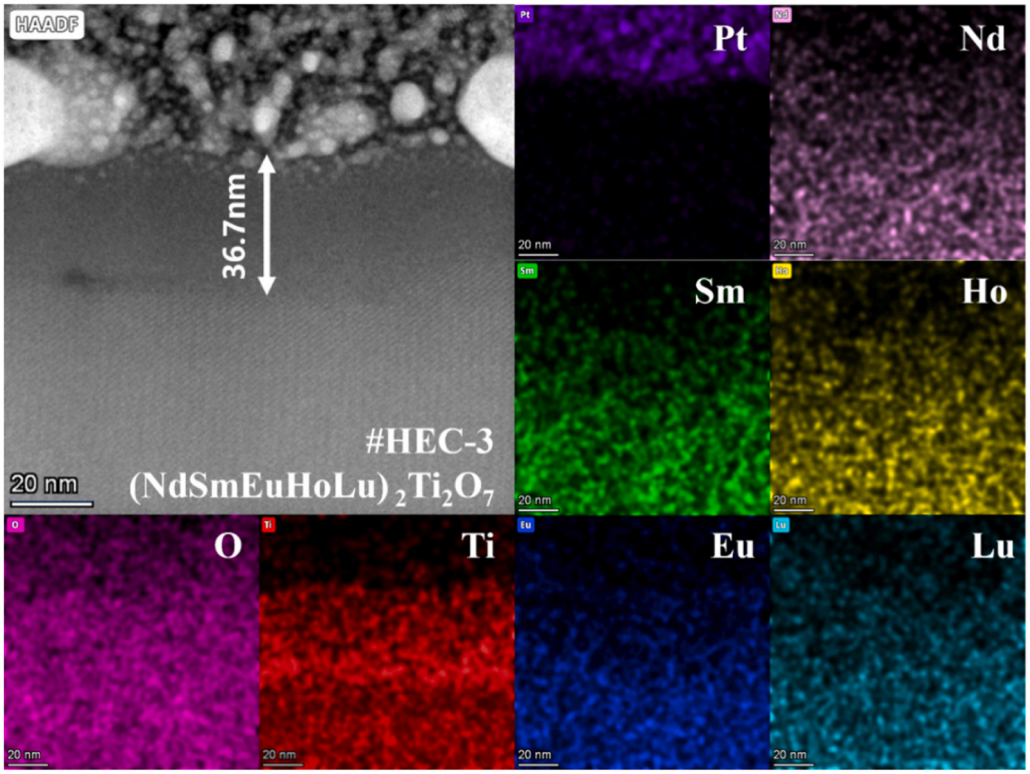

Fig. 6. Elemental Mapping of #HEC-3 via HAADF-STEM and EDS Analysis.

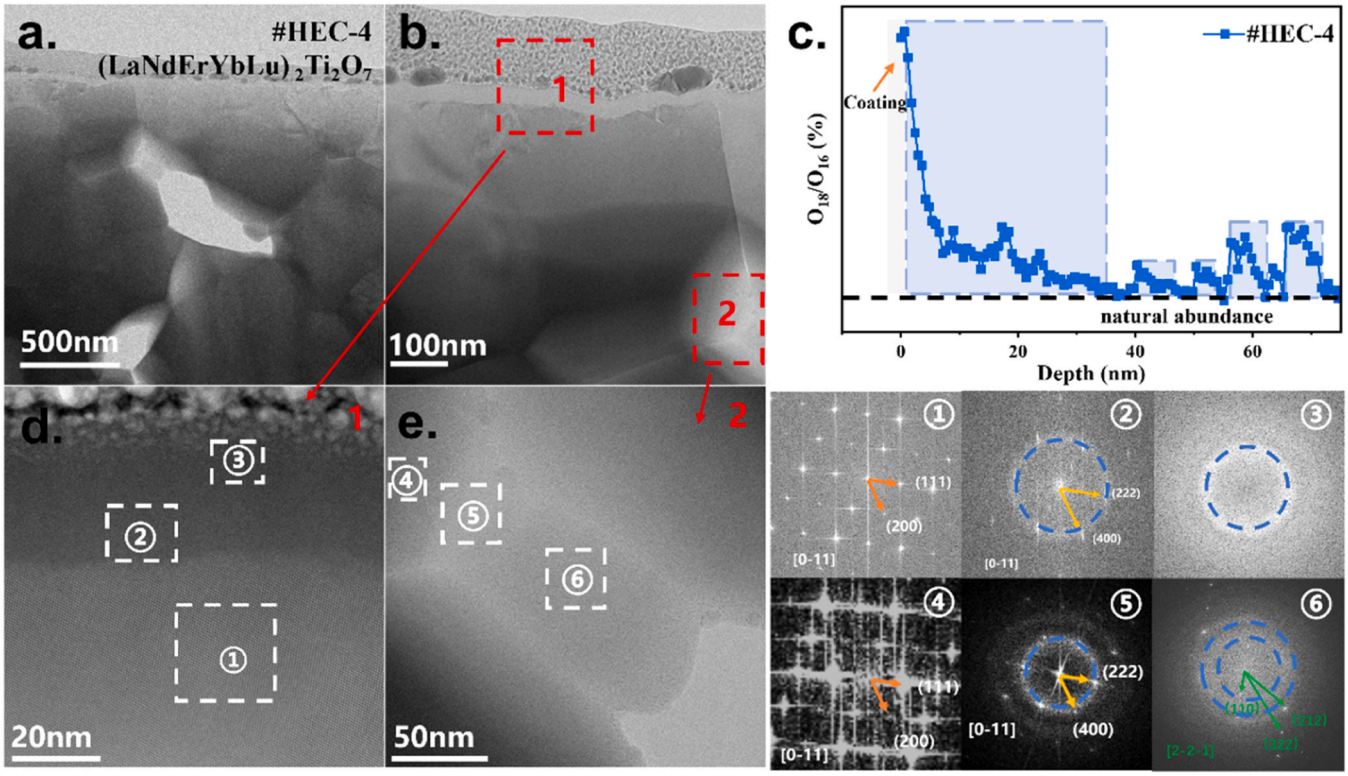

Fig. 7. STEM and TOF-SIMS analysis of the dual crystalline phase #HEC-4: (a-b) Cross-sectional TEM image.(c) $^{18}O/^{16}O$ depth profile across the alteration layer. (d) High-resolution TEM image of alteration layer and corresponding FFT images. (e) High-resolution TEM image across the grain boundary and corresponding FFT images.

In addition, the #HEC-4 with dual crystalline structure suggests a grain dissolution from the monoclinic phase, which further leads to the grain boundary collapse and accelerates the structure degradation (Fig. 7a). The surface passivation film exhibits multiple layers of

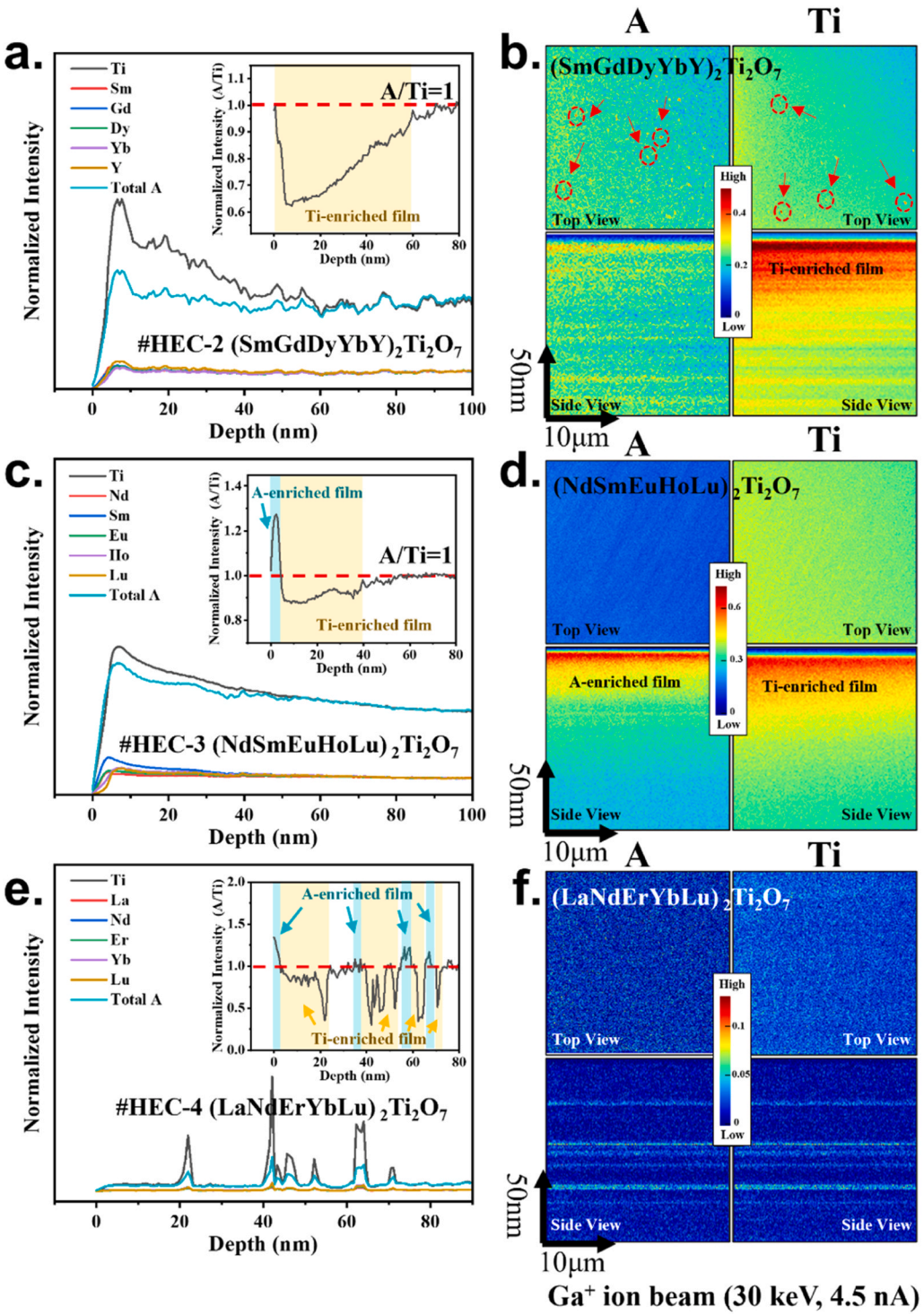

Fig. 8. TOF-SIMS Elemental Depth Profiles (a, b) #HEC-2 with Ti-dominated passivation layer. (c, d) #HEC-3 with Bilayered corrosion interface. (e, f) #HEC-4 with multilayered dissolution with grain boundary collapse.

enriched A/Ti elements inside, which could be tentatively attributed to the preferential dissolution of the monoclinic phase in the biphasic system (Fig. 8e). The porous structure generated simultaneously with the monoclinic dissolution may promote the diffusion of leaching solution into the deep layers of the matrix, potentially triggering corrosion at the grain boundaries of the pyrochlore phase, ultimately leading to a clear interface double-layer interfacial structure (similar to Fig. 8d). It is worth noting that the difference in the depth of monoclinic dissolution might be associated with the appearance of enriched layers at different depths.

3.3. *Chemical durability and leaching mechanisms of HE-$RE_2Ti_2O_7$ ceramics*

The chemical durability of the as-fabricated sample coupons was further studied by semi-dynamic leaching tests for 25 days at 90 ℃ with corresponding A-site leaching rates denoted in Fig. 9a. The single-phase pyrochlore sample (#HEC-2) with low chemical disorder exhibited the

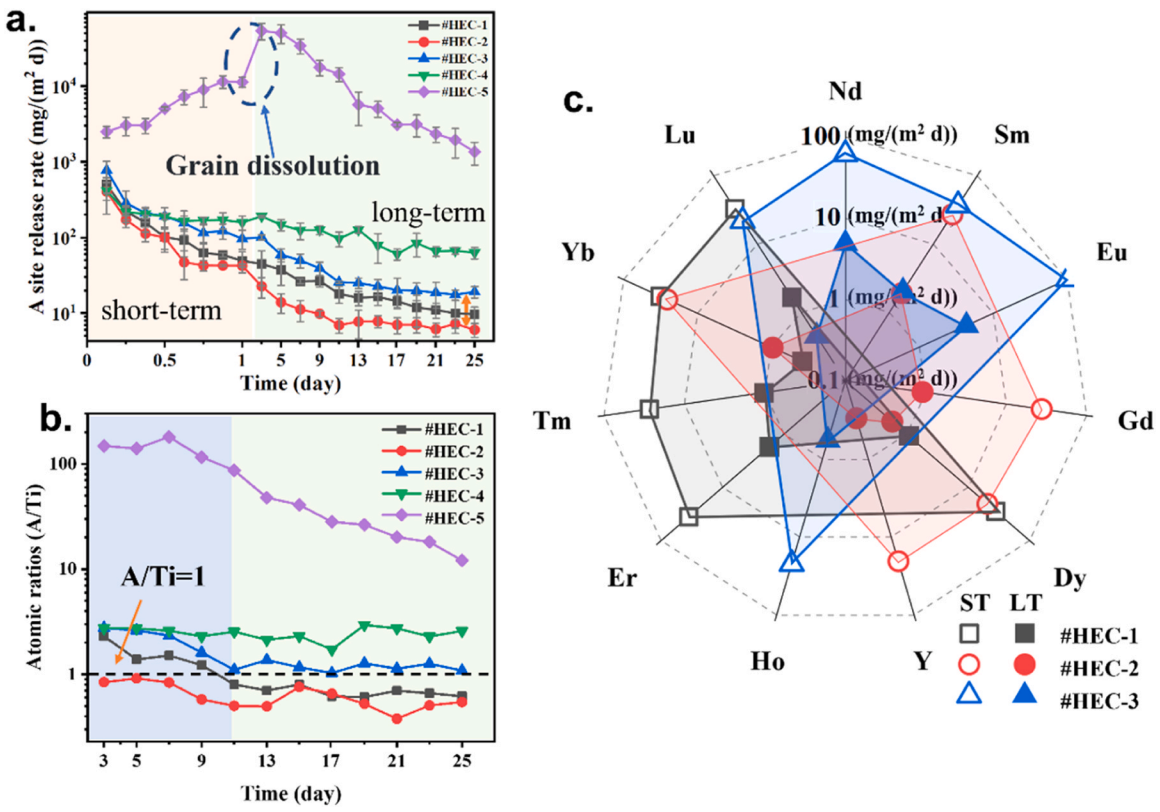

Fig. 9. Leaching mechanism of HE-$RE_2Ti_2O_7$ ceramics (a) A-site element release rates during 25-day leaching tests. (b) A/Ti atomic release ratios over time. (c) Radar chart comparing short-term (ST) and long-term (LT) leaching rates.

lowest elemental release rates, while dual-phase structures showed higher release rates. According to the Transition State Theory (TST), the exponential decay of A-site elements reveals a dissolution mechanism transition: the initial stage is dominated by matrix dissolution, followed by the formation of a surface passivation layer via a dissolution-reprecipitation mechanism, ultimately leading to diffusion-controlled release governed by the passivation layer. Notably, the dual-phase sample #HEC-5 with higher monoclinic phase partition displayed a sharp increase on day-3, attributed to monoclinic phase dissolution-induced grain detachment and subsequent surface area increase.

The #HEC-2 maintained A/Ti ratios below 1, whereas #HEC-3 showed slightly higher ratios exceeding 1 (Fig. 9b). TOF-SIMS analysis (Fig. 8) suggests this differentiation through the characteristics of the surface passivation films: the monolithic Ti-enriched layer in #HEC-2 appears to impede A-site ion migration, while #HEC-3's bilayer structure features an outer A-element-enriched layer formed via dissolution-reprecipitation processes. This phenomenon could arise from the higher $\overline{R}_A$ in #HEC-3, which weakens the A-O bonding strength. Although the surface passivation layer inhibits ion migration, the weakened bonding strength in high chemical disorder systems could potentially outweigh the protective role of the surface film, leading to significant grain boundary collapse.

The short term and long term rates of the A-site elements in high-entropy pyrochlore can be further illustrated in Fig. 9c. The short-term leaching rates for all the five sample coupons are within the same range despite significant differences in ionic radii and metal-oxygen bond strengths. However, significant divergences in long-term leaching rates were observed during the long-term leaching tests, which will be detailed in the following section.

4. Discussion

4.1. Nexus among chemical composition–localized bonding strength–film property

This study suggests the dynamic relationship among chemical composition, localized bonding strength, and passivation film properties in high-entropy pyrochlore with variable chemical disorder (Fig. 10). The chemical composition-induced differences in bonding strength appear to have a significant impact on HE-$RE_2Ti_2O_7$ growth kinetics and film structure. By tailoring A-site rare-earth compositions, a transition from homogeneous Ti-enrich amorphous passivation layers (A/Ti < 1) to heterogeneous bilayer (A-site-enriched/Ti-enriched) structures was achieved.

a. Relationship between Chemical Composition-Dominated Evolution of Bonding Strength

This work suggests that the structural stability of pyrochlore ceramics is closely associated with the metal-oxygen bonding strength (A-O) by configuring the multi-component pyrochlore with the same entropy and different ionic radii [32]. The variations in the ionic radii of A-site cations affect the M–O bond strength based on bond valence theory [33,34], with a reduction in A-O bonding energy by increasing ionic radii (e.g., R_a increases from 0.997 Å to 1.070 Å), leading to lattice expansion (unit cell volume: 1019 $Å^3$ → 1060 $Å^3$) and an increased proportion of monoclinic phase (Fig. 3b), with continuously increasing of the ionic radii will finally result in the 100 % monoclinic structure. The intrinsic relationship between structural stability and dissolution kinetics can be further evidenced by the Raman spectroscopy, where the attenuated intensity of the rare-earth–oxygen (RE–O) vibrational peak at 750 cm^{-1} in the monoclinic phase (Fig. 4d) indicates that weakened A–O bonds accelerate bond breakage during dissolution. These results suggest that chemical composition influences the structural stability of the pyrochlore matrix by adjusting ionic radii and bond strength

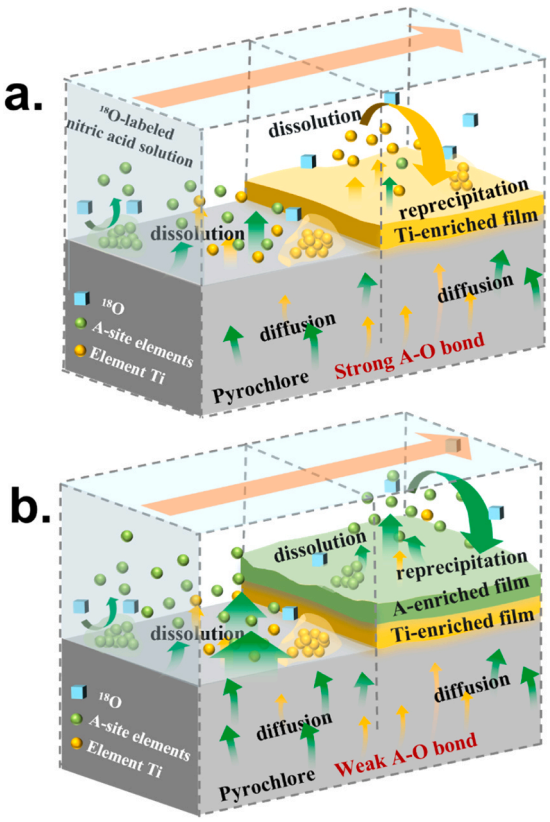

Fig. 10. Elemental Migration Dynamics and Passivation Film Architecture During Pyrochlore Corrosion (a) Schematic of Ti-dominated passivation. (b) Dual-layer passivation with A/Ti differentiation.

variations.

b. Relationship between Bonding Strength and Passivation Layer Formation

The variation in M-O bonding strength governs the bonding breakage in multi-component oxide systems [33]. Cations with weaker bonding strength exhibit preferential dissolution, while those with stronger M–O bonds remain stable. The selective release of A-site elements facilitates the elemental reprecipitation as evidenced in the TOF-SIMS analysis [7, 34].

The potential correlation between average ionic radii and heterogenous passivation film growth mechanism can be further revealed by the TOF-SIMS depth profile. (Fig. 8a). The observed titanium enrichment at the substrate surface (A/Ti < 1) may result from the combined effects of Ti–O bond stability and its low solubility, potentially leading to preferential Ti retention during dissolution-reprecipitation. Reprecipitation occurs even under unsaturated solution conditions considered the low solubility of Ti, ultimately forming a homogeneous Ti-rich amorphous layer (A/Ti < 1), as suggested by previous research [35].

In contrast, it is hypothesized that in high $\overline{R}_A$ systems (e.g., #HEC-3), the interfacial diffusion of A-site elements (e.g., Nd) could be accelerated, due to weakened A–O bonds (Fig. 6). While conventional dissolution-reorganization models predict monolithic Ti-enriched layers, dynamic dissolution-reprecipitation processes enable simultaneous A-site cation participation in passivation film formation, which results in a bilayer film composed of an A-site-enriched outer layer and a Ti-rich inner layer (Fig. 8c). Besides, the isotopic tracing profile ($^{18}O/^{16}O$) indicates a 36.7 nm gradient decay depth profile (Fig. 5c), consistent with the passivation layer thickness denoted from the STEM image, further excluding static surface reconstruction mechanism and implying dissolution-reprecipitation as the likely dominant process.

The growth kinetics of passivation layers are governed by the dynamic competition between interfacial reaction rates and structural evolution. By integrating isotopic tracing (Fig. 5c) and TEM analysis (Fig. 7), the passivation film growth mechanism can be inferred in the schematic diagram in Fig. 10 and summarized below:

Rapid elemental release dominates interfacial reactions during the initial corrosion stage, triggering the preferentially elemental reprecipitation near the substrate, forming a Ti-rich amorphous layer (Figs. 8a-9a). Weakened A-site bonding strength accelerates A-site element release for high $\overline{R}_A$ samples (#HEC-3), which further leads to the rapid localized saturation and reprecipitation of A-site element on the Ti-enriched layer. This process ultimately leads to the formation of a bilayer passivation structure (Fig. 8c). This stage-dependent transformation aligns with Hellmann's Coupled Interface Dissolution-Reprecipitation (CIDR) theory [15]: local supersaturation of dissolved species drives secondary phase nucleation, enabling a kinetic transition from "dissolution-dominated" to "reprecipitation-dominated" regimes.

For comparison, the sample with higher $\overline{R}_A$ (e.g., #HEC-4) featured a dual crystalline structure, suffering from the non-uniform dissolution of monoclinic phases, severely disrupting passivation layer growth kinetics. The rapid dissolution of monoclinic grains generates interconnected pores and large void space across the grain boundary, according to the TEM analysis (Fig. 7a). The large area of grain dissolution can accelerate the ^{18}O diffusion (Fig. 7c) and induce localized dissolution rate spikes (Fig. 9a). The resulting porous network promotes the formation of discontinuous passivation layers at the grain boundary (Fig. 8e), consistent with the dissolution study of $La_2Ti_2O_7$ observed by Yang et al. [4].

4.2. Dynamic controlling of the heterogeneity in the pyrochlore chemical durability

a. Influence of passivation film structure on Chemical Stability

A pronounced decline in the A/Ti atomic release ratio was observed across all the pyrochlore samples after 3 days of leaching period (Fig. 9b), which can be attributed to the gradual formation of surface passivation films. On the other hand, the reduced A/Ti ratio for the dual-phase sample #HEC-5 post-day 3 arises from the distinct leaching kinetics between different phase-structured grains, highlighting the role of phase heterogeneity in controlling the elemental release behavior.

According to transition state theory (TST) [36–38], the leaching process can be divided into three distinct stages: Matrix dissolution-dominated stage: coupling bonding breakage of metal-oxygen bonds drives simultaneously release of both A-site and Ti elements, which initiates the gradual formation of Ti-enriched passivation film due to the dissolution-reprecipitation mechanism, further slow down the elemental dissolution and diffusion. Diffusion-controlled stable stage: The continuous growth of passivation film with gradual coverage on the sample surface leads to the transition to a diffusion-controlled mechanism, further protecting the matrix from corrosion (Fig. 9b). Therefore, the transition between incongruent and congruent mechanisms at day 11, according to the elemental release curves, can be explained by the mechanism transition from stage 2 to stage 3, where the passivation film significantly enhances its barrier effect against A-site leaching.

The differences in dissolution rates among materials (e.g., #HEC-1 to #HEC-5) are governed by the coupling effect between surface passivation film structure and chemical disorder (lattice distortion). Single-phase pyrochlore (#HEC-2) exhibits the lowest long-term dissolution rate due to the formation of a uniform, dense Ti-rich amorphous passivation layer (A/Ti < 1), which effectively suppresses A-site ion migration. In contrast, dual-phase samples (e.g., #HEC-4 and #HEC-5) show significantly higher dissolution rates due to preferential dissolution of the monoclinic phase, leading to grain boundary collapse and porous structures (Fig. 7a), with passivation films exhibiting discontinuous multilayered or fractured features (Fig. 8e). Higher chemical

disorder and weaker bonding strength in #HEC-3 induce a bilayer passivation film (Fig. 8c), resulting in an intermediate dissolution rate. The formation of a dense amorphous film effectively passivates the pyrochlore matrix against further corrosion, substantially improving material durability [39].

b. Heterogeneity in Elemental Release and the underlying dominated mechanism

The short-term leaching rates of A-site elements in the high-entropy pyrochlore are approximately the same during the semi-dynamic leaching tests (outer ring of the radar chart in Fig. 9c), which contradicts the conventional wisdom that the chemical bonding strength dominates the initial rate [11]. This phenomenon could arise from the delayed diffusion effect induced by lattice distortion in high-entropy systems, according to the previous research by Zhou [24]. It is possible that the synergistic interactions among multiple components and the enhanced mixing entropy effectively reduce the release rate by distorting the elemental diffusion throughout the crystalline lattice [40]. Furthermore, an increase in the lattice distortion parameter (δ) could raise the activation energy required for ion migration, which might suppress the initial leaching of large-radius A-site cations (Fig. 9c).

Despite the fact that the surface passivation film strongly impacts the long-term leaching rate, the intrinsic bonding strength among these samples still plays a crucial role in judging the heterogenous elemental release mode as denoted in the leaching curve (Fig. 9a). For instance, the bilayered passivation film structure observed in the #HEC-3 sample shows that larger-radius elements (e.g., Nd) still form an A-site-enriched outer deposition layer despite the protective Ti-rich inner layer. Long-term leaching experiments reveal that A-site elements with larger ionic radii and weaker metal-oxygen bond strengths (e.g., Nd, Sm) exhibit higher release rates, whereas those with smaller radii and stronger bond strengths (e.g., Yb, Lu) show lower rates regardless of the effect of surface passivation film (Fig. 9a). Comparative analysis revealed significant disparities in long-term leaching rates of identical A-site elements across the as-fabricated five high-entropy pyrochlores, with Sm showing notably higher rates in #HEC-3. This divergence is primarily attributed to variations in chemical disorder and the heterogeneous structure of the passivation film.

These findings further suggest the critical mechanism by which the coupling effect of bonding strength, lattice distortion, and surface alteration behavior on the long-term stability of multi-component pyrochlore structure instead of solely dependent on mixing entropy since the mixing entropy is identical for the samples studied herein.

5. Summary and conclusions

This study fabricated the high-entropy pyrochlore with the different chemical disorder and further proposed a potential mechanism for the formation of surface passivation films by establishing an association among chemical composition, passivation film formation, and chemical durability. The key findings can be summarized below:

(1) The surface oxide film formation is likely dominated by a dissolution-reprecipitation mechanism, as suggested by advanced material characterization techniques including the oxygen isotope ($^{18}O/^{16}O$) profiles of TOF-SIMS and TEM analysis.
(2) The chemical composition and microstructure of the surface passivation film are not intrinsic, which may be closely related to the heterogeneous elemental release behavior. It is hypothesized that homogeneous Ti-rich amorphous layers (A/Ti<1) form via preferential Ti-O bond reprecipitation, effectively inhibiting corrosion, while A/Ti bilayered structures may arise from weakened A-O bonds, triggering A-site cation saturation and precipitation to form the outer layer of the passivation film.
(3) The anti-corrosion behavior of pyrochlore is not intrinsic and cannot be solely explained by the entropy effect. The high-entropy effect may be associated with lattice structure changes, potentially involving the suppression of the initial leaching rate of large A-site cations through altered ion diffusion. However, the long term elemental release rates appear to be strongly correlated with localized chemical bonding strength, and surface alteration behavior.

Overall, this work contributes to the foundational understanding of the surface alteration behavior and chemical durability of multi-component pyrochlore solid solutions. Furthermore, the current study offers new experimental and theoretical insights into the corrosion passivation mechanisms of high-entropy materials.

CRediT authorship contribution statement

Hao Ji: Methodology. **Yibo Wang:** Investigation. **Minghao Zhao:** Conceptualization. **yang kun:** Supervision. **Wangwei Ru:** Data curation. **Xiaobin Tang:** Validation. **chen wei:** Data curation.

Declaration of Competing Interest

The authors declare that they have no known competing financial interests or personal relationships that could have appeared to influence the work reported in this paper.

Acknowledgment

The authors would like to express appreciation for financial support from the National Natural Science Foundation of China (No. 37244600) and the Natural Science Foundation of Jiangsu Province (BK20230898); We also thank the Center for Microscopy and Analysis of Nanjing University of Aeronautics and Astronautics for technical assistance.

Appendix A. Supporting information

Supplementary data associated with this article can be found in the online version at doi:10.1016/j.jeurceramsoc.2026.118222.

Data availability

The data will be made available upon request.

References

[1] A.E. Ringwood, V.M. Oversby, S.E. Kesson, W. Sinclair, N. Ware, W. Hibberson, A. Major, Immobilization of high-level nuclear reactor wastes in SYNROC: a current appraisal, Nucl. Chem. Waste Manag. 2 (1981) 287–305, https://doi.org/10.1016/0191-815X(81)90055-3.
[2] S.V. Yudintsev, S.V. Stefanovsky, B.S. Nikonov, A pyrochlore-based matrix for isolation of the REE-actinide fraction of wastes from spent nuclear fuel reprocessing, Dokl. Earth Sc. 454 (2014) 54–58, https://doi.org/10.1134/S1028334X14010152.
[3] U. Schulz, W. Braue, Degradation of $La_2Zr_2O_7$ and other novel EB-PVD thermal barrier coatings by CMAS ($CaO–MgO–Al_2O_3–SiO_2$) and volcanic ash deposits, Surf. Coat. Technol. 235 (2013) 165–173, https://doi.org/10.1016/j.surfcoat.2013.07.029.
[4] K. Yang, P. Lei, T. Yao, B. Gong, Y. Wang, M. Li, J. Wang, J. Lian, A systematic study of lanthanide titanates ($A_2Ti_2O_7$) chemical durability: corrosion mechanisms and control parameters, Corros. Sci. 185 (2021) 109394, https://doi.org/10.1016/j.corsci.2021.109394.
[5] E.H. Oelkers, J. Schott, Thermodynamics and Kinetics of Water-Rock Interaction, in: Reviews in Mineralogy & Geochemistry, 70, Mineralogical Society of America and Geochemical Society, 2009. ISSN 1529-6466.
[6] J.D. Vienna, J.V. Ryan, S. Gin, et al., Current understanding and remaining challenges in modeling long term degradation of borosilicate nuclear waste glasses [J], Int. J. Appl. Glass Sci. 4 (4) (2013) 283–294.
[7] G.S. Frankel, J.D. Vienna, J. Lian, J.R. Scully, S. Gin, J.V. Ryan, J. Wang, S.H. Kim, W. Windl, J. Du, A comparative review of the aqueous corrosion of glasses, crystalline ceramics, and metals, Npj Mater. Degrad. 2 (2018) 1–17, https://doi.org/10.1038/s41529-018-0037-2.
[8] Y. Hu, M. Anandkumar, Y. Zhang, J. Joardar, A.S. Deshpande, X. Wang, K. M. Reddy, High-temperature elemental segregation induced structure degradation in high-entropy fluorite oxide, J. Adv. Ceram. 13 (2024) 310–322, https://doi.org/10.26599/JAC.2024.9220854.

[9] K. Yang, K. Bryce, T. Yao, D. Zhao, J. Lian, Chemical durability and corrosion-induced microstructure evolution of compositionally complex titanate pyrochlore waste forms with uranium incorporation, J. Eur. Ceram. Soc. 44 (2024) 1102–1114, https://doi.org/10.1016/j.jeurceramsoc.2023.09.071.
[10] K. Yang, Y. Wang, J. Shen, S.M. Scott, B.J. Riley, J.D. Vienna, J. Lian, Cs3Bi2I9-hydroxyapatite composite waste forms for cesium and iodine immobilization, J. Adv. Ceram. 11 (2022) 712–728, https://doi.org/10.1007/s40145-021-0565-z.
[11] G.S. Frankel, J.D. Vienna, J. Lian, et al., Recent advances in corrosion science applicable to disposal of high-level nuclear waste, Chem. Rev. 121 (20) (2021) 12327–12383.
[12] J.D. Vienna, J.V. Ryan, S. Gin, et al., Current understanding and remaining challenges in modeling long term degradation of borosilicate nuclear waste glasses, Int. J. Appl. Glass Sci. 4 (4) (2013) 283–294.
[13] M. Herrmann, Corrosion of silicon nitride materials in aqueous solutions, J. Am. Ceram. Soc. 96 (2013) 3009–3022, https://doi.org/10.1111/jace.12509.
[14] A. Janssen, A. Putnis, T. Geisler, C.V. Putnis, The experimental replacement of ilmenite by rutile in HCl solutions, Mineral. Mag. 74 (2010) 633–644.
[15] R. Hellmann, R. Wirth, D. Daval, J.-P. Barnes, J.-M. Penisson, D. Tisserand, T. Epicier, B. Florin, R.L. Hervig, Unifying natural and laboratory chemical weathering with interfacial dissolution–reprecipitation: a study based on the nanometer-scale chemistry of fluid–silicate interfaces, Chem. Geol. 294–295 (2012) 203–216.
[16] S. Gin, L. Neill, M. Fournier, P. Frugier, T. Ducasse, M. Tribet, A. Abdelouas, B. Parruzot, J. Neeway, N. Wall, The controversial role of inter-diffusion in glass alteration, Chem. Geol. 440 (2016) 115–123, https://doi.org/10.1016/j.chemgeo.2016.07.014.
[17] T. Geisler, L. Dohmen, C. Lenting, et al., Real-time in situ observations of reaction and transport phenomena during silicate glass corrosion by fluid-cell Raman spectroscopy, Nat. Mater. 18 (4) (2019) 342–348.
[18] C.M. Rost, E. Sachet, T. Borman, A. Moballegh, E.C. Dickey, D. Hou, J.L. Jones, S. Curtarolo, J.-P. Maria, Entropy-stabilized oxides, Nat. Commun. 6 (2015) 8485.
[19] R. Yan, W. Liang, Q. Miao, H. Zhao, R. Liu, M. Dong, K. Zang, F. Jia, X. Chang, X. He, X. Gao, Y. Song, X. Tao, Corrosion mechanisms of high-entropy rare earth zirconate (Gd0.2Y0.2Er0.2Tm0.2Yb0.2)2Zr2O7 exposed to CMAS and multi-medium (NaVO3+CMAS), J. Eur. Ceram. Soc. 44 (2024) 3277–3295.
[20] M. Qin, H. Vega, D. Zhang, S. Adapa, A.J. Wright, R. Chen, J. Luo, 21-Component compositionally complex ceramics: discovery of ultrahigh-entropy weberite and fergusonite phases and a pyrochlore-weberite transition, J. Adv. Ceram. 11 (2022) 641–655.
[21] Z. Teng, L. Zhu, Y. Tan, S. Zeng, Y. Xia, Y. Wang, H. Zhang, Synthesis and structures of high-entropy pyrochlore oxides, J. Eur. Ceram. Soc. 40 (2020) 1639–1643, https://doi.org/10.1016/j.jeurceramsoc.2019.12.008.
[22] H. Guo, K. Zhang, Y. Li, X. Jiang, Preparation and properties of high-entropy pyrochlore A2Ti2O7 with multi-elements at A site, Ceram. Int. 50 (2024) 1–8, https://doi.org/10.1016/j.ceramint.2023.09.184.
[23] Z. Teng, Y. Tan, S. Zeng, Y. Meng, C. Chen, X. Han, H. Zhang, Preparation and phase evolution of high-entropy oxides A2B2O7 with multiple elements at A and B sites, J. Eur. Ceram. Soc. 41 (2021) 3614–3620, https://doi.org/10.1016/j.jeurceramsoc.2021.01.013.
[24] L. Zhou, F. Li, J.-X. Liu, S.-K. Sun, Y. Liang, G.-J. Zhang, High-entropy A2B2O7-type oxide ceramics: a potential immobilising matrix for high-level radioactive waste, J. Hazard. Mater. 415 (2021) 125596, https://doi.org/10.1016/j.jhazmat.2021.125596.
[25] Z. Teng, W. Feng, S. Zeng, C. Chen, S. Peng, Spark plasma sintering of single-phase high entropy A2Zr2O7 pyrochlore oxides and the aqueous durability analysis, Ceram. Int. 50 (2024) 12852–12858, https://doi.org/10.1016/j.ceramint.2024.01.192.
[26] ASTM C1308-21, Standard Test Method for Accelerated Leach Test for Diffusive Releases from Solidified Waste and a Computer Program to Model Diffusive, Fractional Leaching from Cylindrical Waste Forms, ASTM International, West Conshohocken, PA, 2021.
[27] P.L. Côté, T.W. Constable, A. Moreira, An evaluation of cement-based waste forms using the results of approximately two years of dynamic leaching, Nucl. Chem. Waste Manag. 7 (1987) 129–139, https://doi.org/10.1016/0191-815X(87)90007-6.
[28] K. Bryce, K. Yang, T. Yao, J. Lian, Chemical durability of multicomponent lanthanide zirconate solid solutions, Ceram. Int. 49 (2023) 39196–39204.
[29] K. Krishnankutty, K.R. Dayas, Synthesis and characterization of monoclinic rare earth titanates, RE2Ti2O7 (RE = La, Pr, Nd), by a modified SHS method using inorganic activator, Bull. Mater. Sci. 31 (2008) 907–918, https://doi.org/10.1007/s12034-008-0145-7.
[30] L. Vegard, Die Konstitution der Mischkristalle und die Raumfüllung der Atome, Z. Phys. 5 (1921) 17–26, https://doi.org/10.1007/BF01349680.
[31] C. Wan, Z. Qu, A. Du, W. Pan, Order−disorder transition and unconventional thermal conductivities of the (Sm1−xYbx)2Zr2O7 Series, J. Am. Ceram. Soc. 94 (2011) 345–354, https://doi.org/10.1111/j.1551-2916.2010.04113.x.
[32] J.M. Farmer, L.A. Boatner, B.C. Chakoumakos, M.-H. Du, M.J. Lance, C.J. Rawn, J. C. Bryan, Structural and crystal chemical properties of rare-earth titanate pyrochlores, J. Alloy. Compd. 605 (2014) 63–70, https://doi.org/10.1016/j.jallcom.2014.03.153.
[33] E.H. Oelkers, General kinetic description of multioxide silicate mineral and glass dissolution, Geochim. Et. Cosmochim. Acta 65 (2001) 3703–3719, https://doi.org/10.1016/S0016-7037(01)00710-4.
[34] M.A. Velbel, Bond strength and the relative weathering rates of simple orthosilicates, Am. J. Sci. 299 (1999) 679–696, https://doi.org/10.2475/ajs.299.7-9.679.
[35] C.M. Jantzen, et al., Leaching of polyphase nuclear waste ceramics: microstructural and phase characterization, J. Am. Ceram. Soc. 65 (1982) 292–300, https://doi.org/10.1111/j.1151-2916.1982.tb10447.x.
[36] B. Grambow, A general rate equation for nuclear waste glass corrosion, MRS Online Proc. Libr. 44 (1984) 15–27, https://doi.org/10.1557/PROC-44-15.
[37] P. Aagaard, H.C. Helgeson, Thermodynamic and kinetic constraints on reaction rates among minerals and aqueous solutions; I, theoretical considerations, Am. J. Sci. 282 (1982) 237–257, https://doi.org/10.2475/ajs.282.3.237.
[38] J. Schott, O.S. Pokrovsky, E.H. Oelkers, The link between mineral dissolution/precipitation kinetics and solution chemistry, Rev. Mineral. Geochem. 70 (2009) 207–258, https://doi.org/10.2138/rmg.2009.70.6.
[39] K. Yang, Y. Wang, P. Lei, T. Yao, D. Zhao, J. Lian, Chemical durability and surface alteration of lanthanide zirconates (A2Zr2O7: A = La-Yb), J. Eur. Ceram. Soc. 41 (2021) 6018–6028, https://doi.org/10.1016/j.jeurceramsoc.2021.05.038.
[40] B. Gong, K. Yang, J.A. Lian, J. Wang, Machine learning-enabled prediction of chemical durability of A2B2O7 pyrochlore and fluorite, Comput. Mater. Sci. 200 (2021), https://doi.org/10.1016/j.commatsci.2021.110820.